RSC Advances

ROYAL SOCIETY OF CHEMISTRY

www.rsc.org/advances

Journal Name

RSCPublishing

ARTICLE

Incorporation of PEDOT:PSS into SnO_2/Reduced Graphene Oxide Nanocomposite Anodes for Lithium-Ion Battery to achieve Ultra-High Capacity and Cyclic Stability

Cite this: DOI: 10.1039/x0xx00000x

Received 00th January 2012,
Accepted 00th January 2012

DOI: 10.1039/x0xx00000x

www.rsc.org/

Md. Selim Arif Sher Shah,‡[a] Shoaib Muhammad,‡[b] Jong Hyeok Park,[ac] Won-Sub Yoon*[b] and Pil J. Yoo*[ac]

SnO_2, a candidate material for anodes in Li-ion batteries (LIBs), usually suffers from severe volume changes (> 300%) during charge/discharge cycles. This problem leads to undesirable continuous capacity fading, hindering its practical utilization. To address this issue, nanostructured SnO_2 and its composites with carbon nanomaterials, especially graphene, have extensively been studied. Although the stability issue has improved substantially, these materials still suffer from low capacity characteristics, which are far from the theoretical capacity of SnO_2. Motivated by this background, in this work, we synthesized a novel ternary nanocomposite of SnO_2, reduced graphene oxide (rGO), and a conducting polymer, poly(3,4-ethylenedioxythiophene)-poly(styrenesulfonate) (PEDOT:PSS), as a high performance anode material in LIBs. PEDOT:PSS together with rGO is expected to efficiently accommodate the volume change in SnO_2 during cycling. Transmission electron microscopic observation reveals 2-3 nm-sized SnO_2 nanoparticles are uniformly dispersed over rGO nanosheets while having a PEDOT:PSS coating. The capacities of the synthesized composites were dependent on the PEDOT:PSS concentration. The reversible capacity of the composite with 5 wt% PEDOT:PSS was maintained at 980 mAh/g with a coulombic efficiency over 99% even after 160 cycles. This capacity value is equivalent to 1185 mAh/g on the basis of only SnO_2 in the composite. The high capacity of the ternary nanocomposites is attributed to the ultra-small size of SnO_2 nanoparticles, enhanced electronic and ionic mobility, and facilitated volumetric relaxation synergistically offered by rGO nanosheets and the PEDOT:PSS coating.

Introduction

Since their successful industrial launch in the early 1990s, lithium ion batteries (LIBs) have quickly gained much of the market for consumer electronic devices.[1–4] In particular, to meet a recent need for increased capacity in affordable mobile devices, a variety of non-carbon metallic species, such as Si (~4000 mAh/g)[5–9], Ge (1600 mAh/g)[10–15], and Sn (~992 mAh/g)[16,17], which can incorporate relatively more Li ions into the alloy to attain a high theoretical capacity, have been investigated to replace conventional graphite anodes. In parallel, researchers have sought a suitable oxide material that can store and deliver high energy. Among several materials, SnO_2 is considered as an appealing anode material in LIBs because of its good physical and chemical stability, environmentally-friendly nature, low Li ion intercalation potential, and high theoretical capacity (782 mAh/g, but it may be as high as 1493 mAh/g under totally reversible conditions), which would be about four times greater than that of commercial graphite (specific capacity of 372 mAh/g).[18–24] Moreover, the potential of an SnO_2 anode is also higher than that of graphite; thus, it reduces metallic lithium deposition on the anode during fast charging. However, the main drawback of a SnO_2 anode is its severe volume change (> 300 %) between the fully lithiated and delithiated states. This leads to pulverization and structural collapse of the electrode, eventually resulting in a loss of electrical contacts between SnO_2 particles and the current collector. As a result, continuous capacity fading occurs during cycling.[21,25–27] Although nano-sized SnO_2 can alleviate the pulverization problem to some extent, complete suppression has not yet been accomplished because the particle size below which the pulverization is totally absent is much smaller than the unit cell size of the SnO_2. In addition, agglomeration of primary SnO_2 nanoparticles decreases the binding sites for Li ions, which generates severe mechanical stress and decreases Li ion mobility, ultimately resulting in a loss of capacity.[28–31] Moreover, a pure SnO_2 anode suffers from

low initial coulombic efficiency because of considerable irreversible reaction in the first cycle. Apart from this characteristic, it has been reported that electrochemically active Sn nanoparticles are formed as a result of partial reduction of SnO_2 by Li ions during cycles. However, these Sn nanoparticles generally tend to aggregate into larger, inactive Sn clusters, resulting in deterioration of the reversible capacity of the electrode.[32,33]

Composites of SnO_2 with different carbon nanomaterials may be superior to SnO_2 alone because the carbon materials act as a cushioning layer to buffer against volume change and to improve electrical conductivity of the composites. In this regard, graphene, a single-atom-thick planar carbon nanomaterial, is considered as a promising 2D material due to its excellent electrical conductivity, large surface area (> 2600 m^2/g), and high structural flexibility.[34–36] Therefore, SnO_2-graphene nanocomposites have extensively been studied as a promising anode material for advanced LIBs. However, the problem of pulverization and capacity fading has not been completely eliminated.[37–39] Meanwhile, such a limitation indicates that there is still much room to increase the capacity of such composite systems.

A good strategy to overcome the limitation of SnO_2-graphene composites is to make ternary nanocomposites, in which the third component further accommodates the volume change more efficiently in comparison to the binary composites. There are several reports where nanostructured SnO_2 materials were sandwiched between graphene layers. For example, Prabakar *et al.* reported alternating stacks of SnO_2 with graphene oxide (GO) and amine functionalized graphene, which showed an excellent capacity of 872 mAh/g after 200 cycles at a current density of 100 mA/g.[40] N-doped graphene-SnO_2 sandwiched papers were demonstrated by Wang *et al.*, wherein a capacity over 800 mAh/g at 50 mA/g after 50 cycles and enhanced cycle stability of the composite were reported.[41] The excellent electrochemical behaviour was attributed to the N-doped graphene and optimized structural features. In another report, Sun *et al.* described sandwiched graphene-SnO_2 nanorod-carbon nanostructures for ultra-high lithium storage properties.[4] They achieved a capacity of 1419 mAh/g after 150 cycles at 0.1 C, as compared to 389 mAh/g for graphene-SnO_2 nanorod complexes. Very recently, Bhaskar *et al.* reported ternary composites of SnO_2 hollow spheres with poly(3,4-ethylenedioxythiophene) (PEDOT) and graphene oxide.[42] They reported a capacity of 608 mAh/g at a current density of 100 mA/g after 150 cycles. Since they employed non-electroconductive graphene oxide as a complexing agent instead of graphene or reduced graphene oxide, they obtained a relatively low capacity value. To date, only a few reports have described a capacity that is close to the theoretical value of SnO_2. In this regard, there is an urgent need to develop new electrode materials possessing remarkably enhanced capacities and high rate performance for development of the next-generation LIBs.

In the present work, we report ternary composites of SnO_2 nanoparticles with PEDOT:PSS and reduced graphene oxide (rGO). The composites were synthesized through simple yet robust a one-pot wet chemical method, namely, complexation and precipitation of SnO_2 nanoparticles on rGO under reflux followed by the addition of PEDOT:PSS (Scheme 1). The synthetic conditions are mild, and the maximum temperature of 100°C lasts for 1.5 h, followed by heating at 65°C for 15 h; water is used as the only solvent. Under these synthetic conditions, we obtained small SnO_2 nanoparticles (2–3 nm in size) while excluding the use of surfactants or harsh chemicals. The ultra-small SnO_2 nanoparticles are uniformly distributed over rGO nanosheets and the composites are stably enwrapped with PEDOT:PSS. As a result, the undesirable tendency SnO_2 nanoparticles to self-agglomerate, which allows for restacking of rGO nanosheets, was largely eliminated. Moreover, the ultra-small SnO_2 nanoparticles led to a decrease in the lithium diffusion length, which, together with the efficient accommodation of volume changes of SnO_2 during charge-discharge cycles, ultimately gives rise to high capacity. Accordingly, the ternary nanocomposite shows high lithium storage capacity and excellent capacity retention characteristics, which are much greater than those of SnO_2-based binary composites. The specific capacities of the ternary composites vary depending on the amount of complexed PEDOT:PSS.

Experimental section

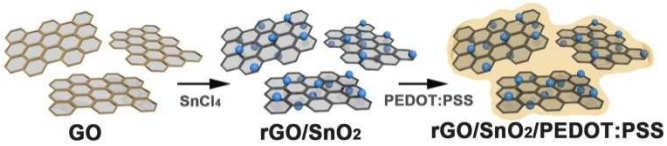

Scheme 1 Synthetic procedure of ternary nanocomposites of rGO/SnO_2/PEDOT:PSS.

Materials

Graphite powder (< 20 μm, synthetic), poly(3,4-ethylenedioxy-thiophene-poly(styrenesulfonate) (PEDOT:PSS) and tin tetrachloride ($SnCl_4$) were purchased from Sigma-Aldrich. $NaNO_3$ (99.0%) was obtained from Yakuri Pure Chemicals Co. Ltd., Japan. H_2SO_4 (95.0%), $KMnO_4$ (99.3%), and H_2O_2 (34.5%) were purchased from Samchun Chemical Co. Ltd., Korea. All the chemicals were used as received and without further purification. In all experiments, deionized water of resistance 18.2 MΩ was used.

Synthesis

GO was synthesized using a modified Hummers' method, which is described elsewhere.[43,44] In a typical synthesis of the ternary composites, 30 ml of a GO (1.5 mg/ml) dispersion in water was mixed with 45 ml deionized (DI) water. The resulting dispersion was sonicated for 1 h and was cooled using ice. Then, 0.15 ml $SnCl_4$ was added drop-wise to the dispersion under vigorous stirring. Gentle stirring was continued for over 1 h while maintaining a temperature below 5°C. The solution was then refluxed in a 250 ml round bottom flask. After 1.5 h, the temperature was decreased to 65°C and PEDOT:PSS was

added. Stirring was continued at that temperature for 15 h more. The dark blue solution was cooled to room temperature and the precipitate was washed with copious amounts of water to remove residual Cl ions. The product was dried at 60°C overnight. Hereafter, samples will be denoted as GSP-*x*, where *x* is the weight % of PEDOT:PSS in the composites. For comparison, SnO_2, rGO/SnO_2 (GS), and SnO_2/PEDOT:PSS (SP) were also synthesized following the same experimental conditions, including the same amount of the reactants, without the addition of GO and/or PEDOT:PSS depending on the type of the composite.

Characterization

Powder X-ray diffraction (XRD) patterns were obtained (D8 Focus, Bruker Instruments, Germany) using Cu Kα radiation (λ = 1.5406 Å) in the 2θ range from 2 to 80° with a step size of 0.02° s^{-1}. The accelerating voltage and the applied current were 40 kV and 40 mA, respectively. Scanning electron microscopy images were collected in a field-emission scanning electron microscope (FESEM, JSM-7600F, JEOL). Transmission electron microscopy was carried out with a TECNAI G2 instrument with an acceleration voltage of 300 kV. FTIR measurements (IFS-66/S, Bruker instrument, Germany) were carried out in transmittance mode in the spectral range of 400–4000 cm^{-1} with a resolution better than 0.1 cm^{-1}. Raman spectra were taken using a Micro-Raman spectrometer system (ALPHA 300M, WITec, Germany). The sample was loaded onto a silica wafer and focused using a 50X objective. The spectra were taken in the range of 1–3000 cm^{-1}. X-ray photoelectron spectroscopy (XPS) characterization was performed (ESCA 2000 instrument, VG Microtech, United Kingdom) using an Al Kα X-ray source. All binding energy values were corrected by calibrating the C 1s peak at 284.6 eV. High resolution peaks were deconvoluted using Gaussian–Lorentzian functions with identical full width at half maxima (fwhm) after a Shirley background subtraction. Photoluminescence data were collected using a Cary Eclipse Fluorescence Spectrophotometer (Agilent Technologies).

Electrode preparation

A slurry was prepared by mixing 70 wt % active material with 15 wt % super P and 15 wt % polyvinylidene fluoride (PVdF, Sigma-Aldrich) with a few drops of N-methyl pyrrolidine (Sigma-Aldrich). The resulting slurry was then coated on a copper foil and dried at 60°C for 10 h in a vacuum oven. Average loading of active material of each electrode prepared was 1.5 mg/cm^2. CR 2032 type coin cells were assembled inside an argon-filled glovebox (O_2 and H_2O concentration ≤ 0.5 ppm) using a metallic lithium foil as the counter/reference electrode, and a piece of Celgard as the separator. The electrolyte was 1.3 M $LiPF_6$ dissolved in a mixture of ethylene carbonate (EC) and dimethyl carbonate (DMC) (3:7, v/v). The discharge/charge cycling tests were carried out at constant current rate of C/10 between 0.005 and 3.0 V using a battery test station (WBCS3000, WonATech Corp). Electronic conductivity of the selective electrodes was determined by electrochemical impedance spectroscopy in a range from 20 mHz to 1 MHz using a multichannel electrochemical workstation (Zive MP2, WonATech Corp).

Results and discussion

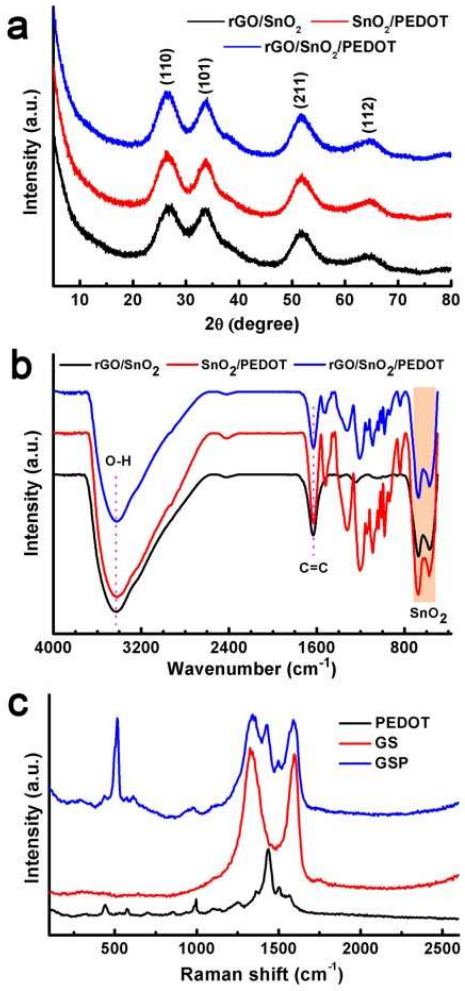

Fig. 1 (a) X-ray diffractograms of SnO_2, GS, and GSP. (b) FTIR spectra of GS, SP, and GSP. (c) Raman spectra of PEDOT:PSS, GS, and GSP.

Crystallographic phases of the synthesized materials were characterized by powder X-ray diffraction measurements. Therein, (110), (101), (211), and (112) planes of SnO_2 were observed respectively, at 2θ values of 26.5, 33.9, 51.8, and 64.9°, as depicted in Fig. 1a.[45] These results confirm that the synthesized SnO_2 is rutile (JCPDS card number 1-625). Unit cell parameters are a = b = 4.688, and c = 3.216 Å.[45] The crystallite size was calculated to be 2.5 nm as determined using the Scherrer formula using (110) planes. These results prove the successful synthesis of ultra-small SnO_2 nanoparticles following a mild synthetic route. X-ray diffractograms of GS and rGO/SnO_2/PEDOT:PSS (GSP) are similar to those of SnO_2. The only difference is that the peaks are broadened in GS and

GSP as compared to SnO_2. Chemical composition of the synthesized materials was confirmed by FTIR analysis. Figure 1b shows FTIR spectra of GS, SP, and GSP. FTIR spectra of GS show C=C and O-H stretching vibrations at 1636 and 3430 cm^{-1}, respectively.[43,44] It further displays two peaks below 800 cm^{-1}, which are due to Sn-O-Sn and O-Sn-O stretching vibrations.[46] Apart from these peaks, the FTIR of SP shows peaks at 1205, 1136 and 1085 cm^{-1} for C-O-C stretching vibrations and peaks at 979, 932, and 842 cm^{-1} for C-S bond stretching of PEDOT:PSS.[42] The FTIR spectrum of GSP is similar to that of SP.

Raman spectral analysis was carried out to provide a detailed understanding of the chemical composition of the synthesized materials. As depicted in Fig. 1c, the Raman spectrum of PEDOT:PSS clearly shows bands at 1568 and 1503 cm^{-1} for the C_α=C_β asymmetric stretching mode, 1430 cm^{-1} for the symmetric C_α=C_β stretching frequency, 1361 cm^{-1} for the C_β-C_β stretching vibration, 1258 cm^{-1} for the C_α-C_α inter-ring stretching mode, 1097 cm^{-1} for C-O-C stretching, 994 and 579 cm^{-1} to oxyethylene ring deformation, 700 cm^{-1} for symmetric C-S-C deformation, and 441 cm^{-1} for SO_2 bending vibration.[47,42] Two main peaks are observed in the Raman spectra of GS at 1331 and 1598 cm^{-1}, which are assigned, respectively, to the D- and G- band of graphene.[48] The ternary composite, GSP, displays all the peaks present in PEDOT:PSS and GS.

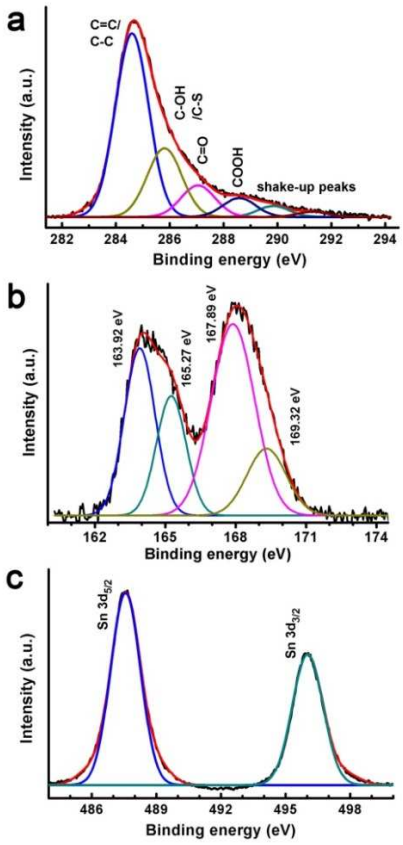

Fig. 2 High resolution XPS spectra of (a) C 1s, (b) S 2p, and (c) Sn 3d of GSP.

X-ray photoelectron spectroscopy was used to further characterize the composites. The survey XPS spectrum of GSP5 (Fig. S1 in the ESI) shows that the composite consists of Sn, C, O and S. Figure 2a shows a high resolution C 1s XPS spectrum of the composite GSP. The peak at 284.6 eV is for the C-C/C=C of graphene.[43] The binding energy of C-OH of graphene and C-S of PEDOT:PSS in the α position is observed at 285.8 eV. C=O of rGO and C=C-O in the β position of PEDOT result in a peak at 287.06 eV.[42] At the same time, the COOH peak of rGO and C-O-C bonding in the ethylene bridge of PEDOT occurs at 288.5 eV. The presence of PEDOT:PSS was further proven by characteristic XPS spectra of S 2p, as depicted in Fig. 2b. Spin-orbit splitting contributions of S 2p in PEDOT were found at 163.9 eV for S $2p_{3/2}$ and at 165.3 eV for S $2p_{1/2}$. Another doublet arises at 167.9 and 169.3 eV, respectively for S $2p_{3/2}$ and S $2p_{1/2}$ of PSS.[49]

The higher energy doublet originated from positively charged sulphur of PSS because a highly electronegative oxygen atom is attached to the S atom. All sulphur contributions have a separation between $2p_{1/2}$ and $2p_{3/2}$ of ~1.4 eV, which is close to the literature values. From the XPS spectrum of S, we can unequivocally conclude that the ternary composite contains PEDOT:PSS. Figure 2c displays high resolution XPS spectra of Sn 3d. As shown, a doublet is observed at 487.6 and 496.0 eV for Sn $3d_{5/2}$ and $3d_{3/2}$, respectively.[41] The separation between the two peaks of the doublet was determined to be 8.4 eV. These observations indicate that Sn is present as Sn^{4+} in the composite, i.e., as SnO_2.

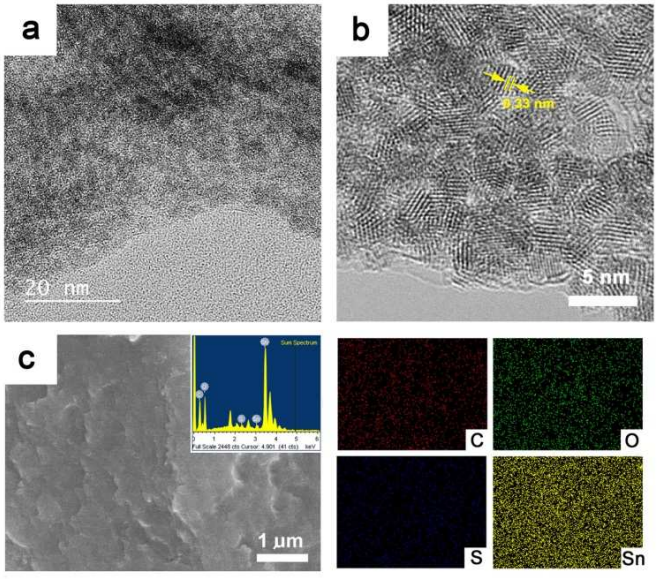

Fig. 3 (a) TEM micrograph of GSP. (b) its HRTEM micrograph. (c) Typical SEM micrograph of the composite. Inset shows its EDS. Elemental mapping for C, O, S and Sn is also shown. For elemental mapping whole area in c was considered.

Figure 3a shows a transmission electron microscope (TEM) image of the composite GSP. From the micrograph, it is evident that 2–3 nm SnO_2 nanoparticles coexist with rGO and PEDOT:PSS. This result, apart from XRD analysis, further confirms the presence of ultra-small SnO_2 nanoparticles in the composites. A high resolution TEM (HRTEM) micrograph of GSP shown in Fig. 3b clearly depicts highly crystalline and ultra-small SnO_2 nanoparticles were obtained following a relatively mild synthetic procedure. TEM micrographs clearly show that the SnO_2 nanoparticles do not form any obvious aggregation. This is an important property, particularly for battery applications, as it mitigates the risk of possible pulverization. Fringe lines with a spacing of 0.33 nm are clearly visible in Fig. 3b, implying (110) planes of rutile SnO_2.[50] Figure 3c is a typical scanning electron microscope (SEM) image of the composite. In the inset in Fig. 3c, an energy dispersive X-ray spectrum (EDS) of the composite is provided, demonstrating that the composite consists of C, O, Sn and S. Elemental mapping is shown on the right side of c. The amount of SnO_2 nanoparticles in the composite was determined by thermogravimetric (TG) analysis. Figure S2 is a TG trace of GSP5 showing that the amount of SnO_2 nanoparticles in the composite is ~ 74 %.

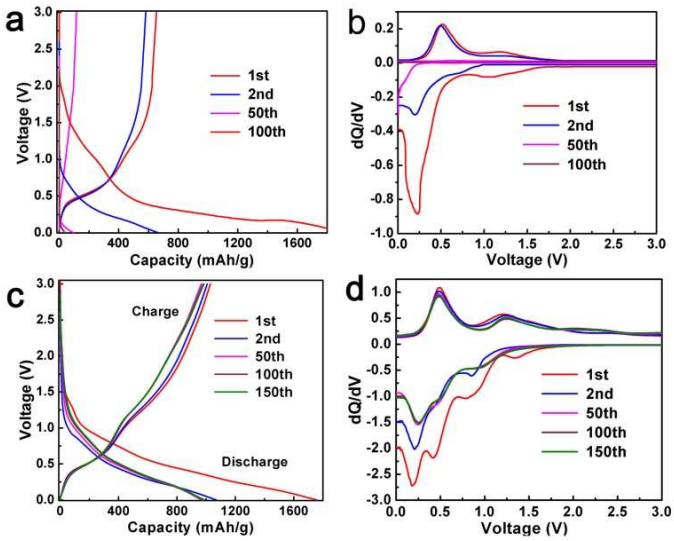

Fig. 4 Charge–discharge profiles and the corresponding differential curves of (a, b) SnO_2 nanoparticles and (c, d) GSP5.

Figure 4a provides voltage curves of the as-synthesized pure SnO_2. The first charge and discharge capacities were 624 and 1916 mAh/g with a coulombic efficiency of merely 32.6%. Other selected voltage profiles for SnO_2 are also shown. Figure 4b represents corresponding differential curves. The differential curves of SnO_2 display two cathodic peaks at 1.05 and 0.22 V; the first peak corresponds to the reduction of SnO_2 to Sn (Reaction 4), while the later peak is due to the alloying of Sn with Li according to Reaction 5 and insertion of Li into rGO (Reaction 6).[51,52] It is notable that there is a shoulder to the broad peak at 1.05 V. This may be due to the formation of a solid electrolyte interface (SEI). It may be noted that, in the second cycle, the reduction peak at 1.05 V disappears and a weak peak arises at 0.72 V, which may be due to the reduction of SnO_2 to Sn. The first anodic cycle shows two peaks at 0.49 and 1.18 V, which are due to de-alloying of Li_xSn and oxidation of Sn to SnO_2. In the second cycle, the oxidation peak at 1.18 V disappears, implying that only the conversion of Sn to Li_xSn occurs in the successive cycles.[52] However, the alloying peak in the cathodic scan and de-alloying peak in the anodic scan exist in the second cycle. After repeated cycles (e.g. 50 times), intensities of all the peaks from both cathodic and anodic processes decrease largely and then nearly disappear after around 100 cycles.

Galvanostatic charge-discharge profiles of the composite anode GSP5 were evaluated in the potential range from 0.005 to 3.0 V vs. Li/Li^+ at a constant current density of 80 mA/g (0.1 C). The first discharge and charge capacity achieved with the cell were 1759 and 1029 mAh/g, as observed in Fig. 4c. Other representative charge–discharge profiles are also shown in Fig. 4c for comparison. To investigate the electrochemical processes occurring during charge-discharge cycles, plots of dQ/dV (known as differential capacity) vs. potential, known as differential curves, are displayed in Fig. 4d. A plateau in the charge-discharge curve appears as a peak in the differential curve. The plot of first discharge (cathodic) cycle exhibits four peaks at 1.32, 0.84, 0.42, and 0.18 V. The peak at 1.32 V indicates the reduction of the electrolyte and formation of a solid electrolyte interface (SEI) at the interface of the electrode and electrolyte. The broad peak at 0.84 V corresponds to the reduction of SnO_2 to SnO and formation of Li_2O. SnO was further reduced to metallic Sn, and Li_2O was formed at 0.42 V.[53] The fourth peak at 0.18 V is due to the alloying of Li and Sn to form Li_xSn ($0 \le x \le 4.4$) and the intercalation of Li^+ ions into rGO. All the reactions occurring at the electrode are given below.

$$\text{Electrolyte} + Li^+ \longrightarrow \text{solid electrolyte interface} \quad (1)$$

$$SnO_2 + 2Li^+ + 2e^- \longrightarrow SnO + Li_2O \quad (2)$$

$$SnO + 2Li^+ + 2e^- \longrightarrow Sn + Li_2O \quad (3)$$

$$SnO_2 + 4Li^+ + 4e^- \longrightarrow Sn + 2Li_2O \quad (4)$$

$$Sn + xLi^+ + xe^- \longrightarrow Li_xSn \quad (0 \le x \le 4.4) \quad (5)$$

$$rGO + xLi^+ + xe^- \longrightarrow Li_xC \quad (6)$$

In the second cycle of the cathodic scan, the peak at 1.32 V disappears. This may be due to the fact that no additional SEI formation occurs on the electrode. All other peaks are present in the successive scans. During the first anodic (charge) scan, two peaks arise at 0.49 and 1.23 V. The oxidation peak at 0.49 V is assigned to the de-alloying of Li_xSn to give rise to Sn and Li, whereas the peak at 1.23 V is due to the oxidation of Sn to

SnO and SnO_2. The reversible capacity of SnO_2 (determined to be 782 mAh/g) is on the basis of the reversibility of Reaction (5). However, we observe that the anodic peak at 1.23 V is present in all the cycles, and the intensity of the peak increases after 100 cycles. This experimental fact implies that Reaction (4) is also reversible, at least to some extent, and it contributes to the extra capacity of SnO_2 in the composites.[25,31,54,55] Apart from this, a new peak at 2.29 V emerges in the anodic scans after the second cycle. In contrast, it is obvious from Fig. 4b that Reaction 4 is not reversible for the SnO_2-only anode.

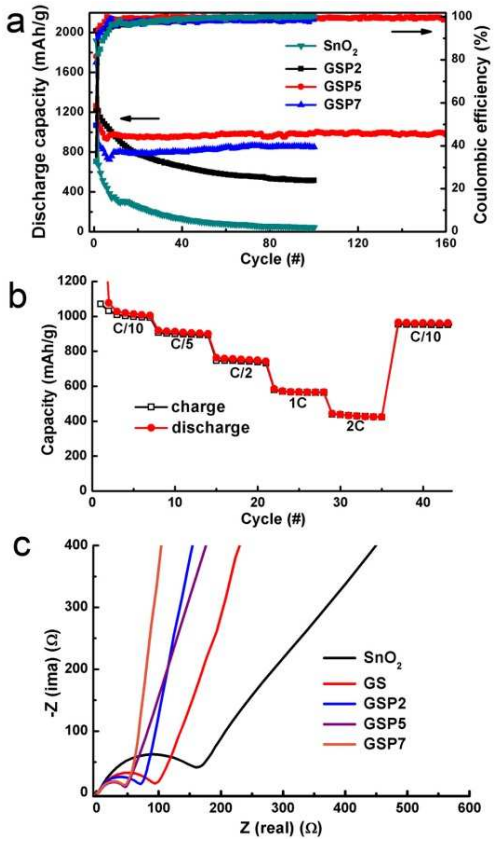

Fig. 5 (a) Galvanostatic cycle performance plots of SnO_2 and its ternary composites at 0.1C in the potential range of 0.005 – 3.0 V vs. Li/Li^+. (b) Rate performance of the composite GSP5. (c) EIS plots of SnO_2, GS and GSP5

The cycling stability of the composites was studied at a constant current density of 80 mA/g (0.1C) in the potential range of 0.005 to 3.0 V vs. Li/Li^+, as shown in Fig. 5. For a comparison, the performance of pure SnO_2 was also observed under the same experimental conditions. Pure SnO_2 shows first charge and discharge capacities of 624 and 1916 mAh/g with a coulombic efficiency of merely 32.6%. The capacity of SnO_2 fades continuously and preserves a discharge capacity of 42 mAh/g after 100 cycles. A binary composite of SnO_2 and GS shows better performance compared to pure SnO_2. The initial discharge capacity of GS is 2071 mAh/g, which, after continuous decay, ends up being 476 mAh/g after 100 cycles, as depicted in Fig. S3. The low capacity value of GS is consistent with results from other reports.[42,56,57]

Figure S3 further shows the discharge capacities of the composites from SP. The initial discharge capacities of the composites GSP2, GSP5, and GSP7 are respectively, 2015, 1759, and 1699 mAh/g, whereas the charge capacities are 1145, 1029, and 839 mAh/g, respectively. The coulombic efficiency values of the GSP2, GSP5, and GSP7 composites are 49.9, 58.5 and 49.4%, respectively. Low values of the coulombic efficiencies of first cycles may be due to the irreversible conversion of SnO_2 to Sn and Li_2O and the formation of SEI on the surface of the active material.[40] The charge-discharge data of GS and SP5 are provided in the ESI. Comparison of charge-discharge characteristics of all samples clearly demonstrate that the ternary composites, especially those with a high concentration of PEDOT:PSS (> 2 wt%), show stable capacity from ~ 10 cycles. This was further proved by the charge-discharge characteristics of GSP10 in Fig. S4, which shows stable capacity from the 10th cycle. The GSP10 composite shows a specific capacity of 709 mAh/g after 229 cycles with a coulombic efficiency >99%. It is notable that the specific capacity of the ternary composites increases first, then decreases with increasing amounts of PEDOT:PSS. The initial capacity loss in these electrodes is mainly due to the formation of SEI. Note that the capacity values were calculated on the basis of the total mass of each electrode. It is obvious that all the composites exhibit higher capacity than pure SnO_2, and the ternary composites display even better capacity than the binary composites of GS or SP.

Notably, the composite GS is better in retaining the capacity compared to the composite SP. The severe capacity fading in SnO_2, GS, and SP may be attributed to the pulverization of the electrodes. However, addition of PEDOT:PSS in GS increases the capacity of the ternary composites first and then decreases the capacity depending on the concentration of PEDOT:PSS. Capacity fading took place even with composite GSP2, which was not as severe as that with SnO_2, GS and SP. The discharge capacity of GSP2 after 100 cycles was 515 mAh/g. On the other hand, composites GSP5 and GSP7 show stable capacity from about 10 cycles. Therefore, we can conclude that the rGO together with PEDOT:PSS efficiently accommodate the volume change (> 300%) of SnO_2 during the charge-discharge process, leading to stable capacity. The composite GSP5 shows a reversible capacity of about 974 mAh/g after 160 charge-discharge cycles with a coulombic efficiency over 99%, indicating that a highly reversible capacity of 1176 mAh/g can be achieved for SnO_2 in the composite. This capacity is almost greater than by a factor of three than the commercial graphite anode, which shows a reversible capacity of 372 mAh/g. Moreover, it is close to the reversible capacity of 1494 mAh/g for SnO_2. On the other hand, GSP7 shows a discharge capacity of 851 mAh/g after 100 cycles, with a coulombic efficiency ~99%. Good rate performance is essential for Li ion batteries. The rate

performance of the composite is depicted in Fig. 5b, which shows that the composite exhibits excellent rate performance at different current densities. Even at high current densities of 1 C and 2 C, the composite delivers specific capacity values of 566 and 424 mAh/g at the seventh cycle, respectively. Moreover, the specific capacity can recover to 962 mAh/g when the current density returned to C/10.

Electrochemical impedance spectra (EIS) data for SnO_2, SP, GSP2, GSP5, and GSP7 were collected and are shown in Fig. 5c. The EIS plots show semi-circles in the high frequency region and sloping straight lines at low frequencies. From these plots, it is clear that the ternary composites GSP5 and GSP7 show minimum charge-transfer resistance, which is due to the presence of highly conducting rGO and intimate contact of SnO_2 nanoparticles with rGO and the conducting polymer PEDOT:PSS. Although their impedance values differ marginally, the composite of GSP5 displays more capacity than GSP7. It is notable that the impedance values of all the ternary composites are lower than that of GS due to the inclusion of PEDOT:PSS. Due to this reason together with insufficient cushioning to volume change, GS shows continuous capacity fading. On the other hand, SnO_2 shows the highest charge-transfer resistance. From the above mentioned discussion, we can conclude that the high specific capacity of the composite GSP5 is obtained due to the following three aspects: i) the ultra-small size of SnO_2 nanoparticles, which decreases the lithium diffusion length in the composite matrix and partially accommodates volume change during charge-discharge cycling, eventually leading to the increased specific capacity, ii) the highly conducting medium provided by rGO and PEDOT:PSS provides low charge-transfer resistance, and iii) efficient buffering capability against volume change offered by the inclusion of rGO and PEDOT:PSS.

Conclusions

Ternary composites of SnO_2 with reduced graphene oxide and PEDOT:PSS were synthesized through a one-pot wet chemical process under mild experimental conditions. In the composites, SnO_2 nanoparticles are in the size range of 2–3 nm, and rGO acted as the conducting medium and buffering matrix to accommodate the volume change. In addition, PEDOT:PSS further contributed to buffer the volume change and increase the conductivity, though the increased addition of PEDOT:PSS could decrease the composite conductivity. The composites showed higher lithium storage capability than pure SnO_2 or the binary composites GS and SP. Moreover, they showed a remarkable coulombic efficiency > 99%. This was possibly due to the efficient accommodation of the severe volume change of SnO_2 by the PEDOT:PSS coating besides the incorporation of rGO. Apart from this, the ultra-small SnO_2 nanoparticles decreased the lithium diffusion length in the composite, leading to high specific capacity. Employing only the rGO or PEDOT:PSS is not sufficient to alleviate the volume change of SnO_2 during charge/discharge cycles. As a result, specific capacities of the ternary composites first increased with the amount of PEDOT:PSS and then decreased. The best capacity was shown by the composite containing 5 wt% PEDOT:PSS, which exhibited a specific capacity of 980 mAh/g, equivalent to 1185 mAh/g with respect to the case of SnO_2 only,, after 160 cycles at a current density of 0.1 C. Moreover, it showed stable capacity at high current densities. We anticipate that the presented approach utilizing ternary composite system can replace commercial graphite anodes in lithium ion battery applications.

Acknowledgements

This work was supported by research grants of NRF (2012M1A2A2671795, 2010-C1AAA001-2010-0029065), Global Frontier R&D Program on Center for Multiscale Energy System (2012M3A6A7055540), funded by the National Research Foundation under the Ministry of Science, ICT & Future, Korea. This work was also supported by Fundamental R&D Program for Technology of World Premier Materials funded by the Ministry of Trade, Industry & Energy of Korea.

Notes and references

[a] *School of Chemical Engineering,* [b] *Department of Energy Science,* [c] *Sungkyunkwan Advanced Institute of Nanotechnology, Sungkyunkwan University, Suwon 440-746, Republic of Korea.*
Corresponding authors: wsyoon@skku.edu (WSY) and pjyoo@skku.edu (PJY)

† Electronic Supplementary Information (ESI) available: Survey XPS spectrum and thermo gravimetric analysis are shown in Fig. S1 and S2, respectively. Fig. S3 depicts cycle performance of GS and SP5. On the other hand, charge/discharge performance and coulombic efficiency of GSP10 is displayed in Fig. S4. See DOI: 10.1039/b000000x/

‡ The authors contributed equally to this work

1. S. R. Gowda, V. Pushparaj, S. Herle, G. Girishkumar, J. G. Gordon, H. Gullapalli, X. Zhan, P. M. Ajayan, and A. L. M. Reddy, *Nano Lett.*, 2012, **12**, 6060–5.
2. a R. Park, J. S. Kim, K. S. Kim, K. Zhang, J. Park, J. H. Park, J. K. Lee, and P. J. Yoo, *ACS Appl. Mater. Interfaces*, 2014, **6**, 1702–8.
3. D. Deng, M. G. Kim, J. Y. Lee, and J. Cho, *Energy Environ. Sci.*, 2009, **2**, 818.
4. D. Wang, J. Yang, X. Li, D. Geng, R. Li, M. Cai, T.-K. Sham, and X. Sun, *Energy Environ. Sci.*, 2013, **6**, 2900.
5. H. Ghassemi, M. Au, N. Chen, P. A. Heiden, and R. S. Yassar, *ACS Nano*, 2011, **5**, 7805–11.
6. H. Li, C. Lu, and B. Zhang, *Electrochim. Acta*, 2014, **120**, 96–101.
7. B. Wang, X. Li, X. Zhang, B. Luo, Y. Zhang, and L. Zhi, *Adv. Mater.*, 2013, **25**, 3560–5.
8. R. Yi, F. Dai, M. L. Gordin, S. Chen, and D. Wang, *Adv. Energy Mater.*, 2013, **3**, 295–300.
9. M. Wu, J. E. C. Sabisch, X. Song, A. M. Minor, V. S. Battaglia, and G. Liu, *Nano Lett.*, 2013, **13**, 5397–402.
10. H. Lee, H. Kim, S.-G. Doo, and J. Cho, *J. Electrochem. Soc.*, 2007, **154**, A343.
11. W. Li, J. Zheng, T. Chen, T. Wang, X. Wang, and X. Li, *Chem. Commun. (Camb).*, 2014, **50**, 2052–4.
12. G. H. Yue, X. Q. Zhang, Y. C. Zhao, Q. S. Xie, X. X. Zhang, and D. L. Peng, *RSC Adv.*, 2014, **4**, 21450.
13. H. Kim, Y. Son, C. Park, J. Cho, and H. C. Choi, *Angew. Chem. Int. Ed. Engl.*, 2013, **52**, 5997–6001.

14. H. Lee, M. G. Kim, C. H. Choi, Y.-K. Sun, C. S. Yoon, and J. Cho, *J. Phys. Chem. B*, 2005, **109**, 20719–23.
15. Y. Liu, S. Zhang, and T. Zhu, *ChemElectroChem*, 2014, **1**, 706–713.
16. E. G. Bae, Y.-H. Hwang, and M. Pyo, *Bull. Korean Chem. Soc.*, 2013, **34**, 1199–1204.
17. X. Hou, H. Jiang, Y. Hu, Y. Li, J. Huo, and C. Li, *ACS Appl. Mater. Interfaces*, 2013, **5**, 6672–7.
18. S. Baek, S.-H. Yu, S.-K. Park, A. Pucci, C. Marichy, D.-C. Lee, Y.-E. Sung, Y. Piao, and N. Pinna, *RSC Adv.*, 2011, **1**, 1687.
19. C.-M. Chen, Q. Zhang, J.-Q. Huang, W. Zhang, X.-C. Zhao, C.-H. Huang, F. Wei, Y.-G. Yang, M.-Z. Wang, and D. S. Su, *J. Mater. Chem.*, 2012, **22**, 13947.
20. S. Chen, M. Wang, J. Ye, J. Cai, Y. Ma, H. Zhou, and L. Qi, *Nano Res.*, 2013, **6**, 243–252.
21. X.-T. Chen, K.-X. Wang, Y.-B. Zhai, H.-J. Zhang, X.-Y. Wu, X. Wei, and J.-S. Chen, *Dalton Trans.*, 2014, **43**, 3137–43.
22. Z. Chen, M. Zhou, Y. Cao, X. Ai, H. Yang, and J. Liu, *Adv. Energy Mater.*, 2012, **2**, 95–102.
23. Y.-L. Ding, Y. Wen, P. a van Aken, J. Maier, and Y. Yu, *Nanoscale*, 2014, **6**, 11411–8.
24. Q. Guo and X. Qin, *ECS Solid State Lett.*, 2013, **2**, M41–M43.
25. F. Han, W.-C. Li, M.-R. Li, and A.-H. Lu, *J. Mater. Chem.*, 2012, **22**, 9645.
26. X. Huang, X. Zhou, L. Zhou, K. Qian, Y. Wang, Z. Liu, and C. Yu, *Chemphyschem*, 2011, **12**, 278–81.
27. Q. Guo, Z. Zheng, H. Gao, J. Ma, and X. Qin, *J. Power Sources*, 2013, **240**, 149–154.
28. H. Kim, S.-W. Kim, Y.-U. Park, H. Gwon, D.-H. Seo, Y. Kim, and K. Kang, *Nano Res.*, 2010, **3**, 813–821.
29. J. G. Kim, S. H. Nam, S. H. Lee, S. M. Choi, and W. B. Kim, *ACS Appl. Mater. Interfaces*, 2011, **3**, 828–35.
30. K. Kisu, M. Iijima, E. Iwama, M. Saito, Y. Orikasa, W. Naoi, and K. Naoi, *J. Mater. Chem. A*, 2014, **2**, 13058.
31. J. Li, Y. Zhao, N. Wang, and L. Guan, *Chem. Commun. (Camb).*, 2011, **47**, 5238–40.
32. Y.-D. Ko, J.-G. Kang, J.-G. Park, S. Lee, and D.-W. Kim, *Nanotechnology*, 2009, **20**, 455701.
33. F. Li, J. Song, H. Yang, S. Gan, Q. Zhang, D. Han, A. Ivaska, and L. Niu, *Nanotechnology*, 2009, **20**, 455602.
34. P. Lian, J. Wang, D. Cai, L. Ding, Q. Jia, and H. Wang, *Electrochim. Acta*, 2014, **116**, 103–110.
35. J. Lin, Z. Peng, C. Xiang, G. Ruan, Z. Yan, D. Natelson, and J. M. Tour, *ACS Nano*, 2013, **7**, 6001–6.
36. J. Liang, W. Wei, D. Zhong, Q. Yang, L. Li, and L. Guo, *ACS Appl. Mater. Interfaces*, 2012, **4**, 454–9.
37. J. Liang, Y. Zhao, L. Guo, and L. Li, *ACS Appl. Mater. Interfaces*, 2012, **4**, 5742–8.
38. Y.-M. Lin, R. K. Nagarale, K. C. Klavetter, A. Heller, and C. B. Mullins, *J. Mater. Chem.*, 2012, **22**, 11134.
39. G. Liu, H. Wang, B. Jin, Z. Yang, W. Qi, Y. Liu, and Q. Jiang, 2013, **8**, 4797–4806.
40. S. J. R. Prabakar, Y.-H. Hwang, E.-G. Bae, S. Shim, D. Kim, M. S. Lah, K.-S. Sohn, and M. Pyo, *Adv. Mater.*, 2013, **25**, 3307–12.
41. X. Wang, X. Cao, L. Bourgeois, H. Guan, S. Chen, Y. Zhong, D.-M. Tang, H. Li, T. Zhai, L. Li, Y. Bando, and D. Golberg, *Adv. Funct. Mater.*, 2012, **22**, 2682–2690.
42. A. Bhaskar, M. Deepa, M. Ramakrishna, and T. N. Rao, *J. Phys. Chem. C*, 2014, **118**, 7296–7306.
43. M. S. A. Sher Shah, A. R. Park, K. Zhang, J. H. Park, and P. J. Yoo, *ACS Appl. Mater. Interfaces*, 2012, **4**, 3893–901.
44. M. S. A. Sher Shah, K. Zhang, a R. Park, K. S. Kim, N.-G. Park, J. H. Park, and P. J. Yoo, *Nanoscale*, 2013, **5**, 5093–101.
45. X. Zhou, L.-J. Wan, and Y.-G. Guo, *Adv. Mater.*, 2013, **25**, 2152–7.
46. H. Seema, K. Christian Kemp, V. Chandra, and K. S. Kim, *Nanotechnology*, 2012, **23**, 355705.
47. A. a. Farah, S. a. Rutledge, A. Schaarschmidt, R. Lai, J. P. Freedman, and A. S. Helmy, *J. Appl. Phys.*, 2012, **112**, 113709.
48. M. S. A. Sher Shah, W.-J. Kim, J. Park, D. K. Rhee, I.-H. Jang, N.-G. Park, J. Y. Lee, and P. J. Yoo, *ACS Appl. Mater. Interfaces*, 2014.
49. W. Zhang, B. Zhao, Z. He, X. Zhao, H. Wang, S. Yang, H. Wu, and Y. Cao, *Energy Environ. Sci.*, 2013, **6**, 1956.
50. S. Paek, E. Yoo, and I. Honma, *Nano Lett.*, 2009, **9**, 72–5.
51. R. Demir-Cakan, Y. Hu, M. Antonietti, J. Maier, and M. Titirici, *Chem. Mater.*, 2008, **20**, 1227–1229.
52. S. Yang, W. Yue, J. Zhu, Y. Ren, and X. Yang, *Adv. Funct. Mater.*, 2013, **23**, 3570–3576.
53. Y. Jiang, T. Yuan, W. Sun, and M. Yan, *ACS Appl. Mater. Interfaces*, 2012, **4**, 6216–20.
54. P. Lian, X. Zhu, S. Liang, Z. Li, W. Yang, and H. Wang, *Electrochim. Acta*, 2011, **56**, 4532–4539.
55. H. Kim, G. O. Park, Y. Kim, S. Muhammad, J. Yoo, M. Balasubramanian, Y. Cho, M.-G. Kim, B. Lee, K. Kang, H. Kim, J. M. Kim, and W. Yoon, *Chem. Mater.*, 2014, **26**, 6361–6370.
56. Y. Tang, D. Wu, S. Chen, F. Zhang, J. Jia, and X. Feng, *Energy Environ. Sci.*, 2013, **6**, 2447.
57. X. Jiang, X. Yang, Y. Zhu, K. Fan, P. Zhao, and C. Li, *New J. Chem.*, 2013, **37**, 3671.

A table of contents entry

A conducting polymer matrix of PEDOT:PSS is incorporated to SnO2/reduced graphene oxide composite for increasing the stability of lithium-ion battery anodes.